

See discussions, stats, and author profiles for this publication at: <https://www.researchgate.net/publication/279163477>

Synthesis of Oligosaccharide-Based Block Copolymers with Pendent Conjugated Oligofluorene Moieties and Their Electrical Device Applications

ARTICLE *in* MACROMOLECULES · JUNE 2015

Impact Factor: 5.8 · DOI: 10.1021/acs.macromol.5b00651

READS

56

8 AUTHORS, INCLUDING:



Wen-Ya Lee

National Taipei University of Technology

60 PUBLICATIONS 1,437 CITATIONS

[SEE PROFILE](#)



Toshifumi Satoh

Hokkaido University

231 PUBLICATIONS 2,978 CITATIONS

[SEE PROFILE](#)



Toyoji Kakuchi

Hokkaido University

331 PUBLICATIONS 4,397 CITATIONS

[SEE PROFILE](#)



Wen-Chang Chen

National Taiwan University

274 PUBLICATIONS 6,911 CITATIONS

[SEE PROFILE](#)

Synthesis of Oligosaccharide-Based Block Copolymers with Pendent π -Conjugated Oligofluorene Moieties and Their Electrical Device Applications

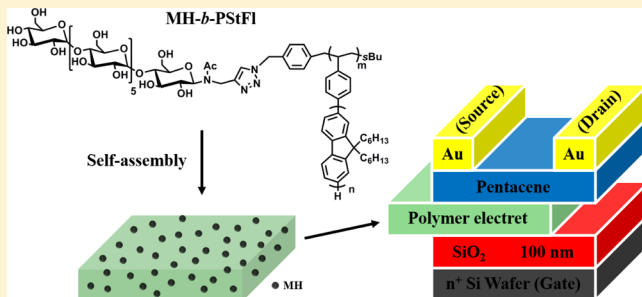
Han-Sheng Sun,[†] Yu-Cheng Chiu,[†] Wen-Ya Lee,[†] Yougen Chen,[‡] Akira Hirao,[†] Toshifumi Satoh,[‡] Toyoji Kakuchi,[‡] and Wen-Chang Chen^{*,†}

[†]Department of Chemical Engineering, National Taiwan University, Taipei, Taiwan 10617

[‡]Division of Biotechnology and Macromolecular Chemistry, Faculty of Engineering, Hokkaido University, Sapporo 060-8628, Japan

Supporting Information

ABSTRACT: We report the synthesis and electric device applications of oligosaccharide-based diblock copolymers consisting of a maltoheptaose (MH) block and a poly(4-oligofluorenylstyrene) block ($PStFl_n$, $n = 1$ or 2), referred to as $MH-b-PStFl_n$. $MH-b-PStFl_n$ was prepared by the Cu(I)-catalyzed click reaction of azido-terminated $PStFl_n$ ($PStFl_n-N_3$), which was obtained from the azidation reaction of the bromo-terminated $PStFl_n$ ($PStFl_n-Br$), with excess ethynyl-terminated MH in the THF/DMF mixture solvent. The resulting diblock copolymers self-assembled to spherical microdomains with sub-10 nm sizes in both bulk and thin film state after annealing process. Thereafter, the $MH-b-PStFl_n$ thin film (~50 nm) with the self-assembled nanoscale spherical aggregates was used as the charge storage layer for the pentacene-based field-effect transistor type memory devices. The $MH-b-PStFl_n$ -based devices had the excellent hole mobility ($0.25\text{--}0.52\text{ cm}^2\text{ V}^{-1}\text{ s}^{-1}$) and the high ON/OFF current (I_{ON}/I_{OFF}) ratio of $10^7\text{--}10^8$, of which the $MH-b-PStFl_1$ -based one had the higher mobility than that of the $MH-b-PStFl_2$ -based one because the pentacene crystal in the former device possessed the larger grain size and fewer boundaries. On the other hand, the $MH-b-PStFl_2$ -based device showed a larger memory window than the $MH-b-PStFl_1$ -based one because the stronger electron-donating effect of the difluorenyl group in $MH-b-PStFl_2$ increased the charge storage capability of its related device. All the memory devices showed a long-term retention time over 10^4 s with the high I_{ON}/I_{OFF} ratio of $10^6\text{--}10^8$. Among these devices, the $MH-b-PStFl_1$ -based device showed a good WRER endurance over 180 cycles. This work not only demonstrates the tunable electrical memory characteristics by adjusting the π -conjugation length of the oligofluorenyl side chain in the polymer electret but also provides a promising approach for developing the next-generation “green electronics” using natural materials.



INTRODUCTION

Carbohydrate polymer, e.g., cellulose, is one of the most abundant natural polymers on the earth, which makes it being a green sustainable source for diverse applications, especially in the fields of biology and medicine due to its environmentally friendly and biocompatible nature. To fully explore its potentials, many efforts have recently been made in some rarely reported fields, such as electronic devices.¹ In general, the realization of these novel functions crucially depends on the phase separation behavior of the carbohydrate-incorporated materials. For example, carbohydrate-based block copolymers can easily self-assemble into a variety of well-ordered periodic nanostructures including sphere, lamellae, hexagonally packed cylinder, and body-centered cubic sphere with sub-10 nm dimension scales.² Nevertheless, the utilization of such carbohydrate-based block copolymers in electronics and optics is obviously insufficient and remains a challenging task.

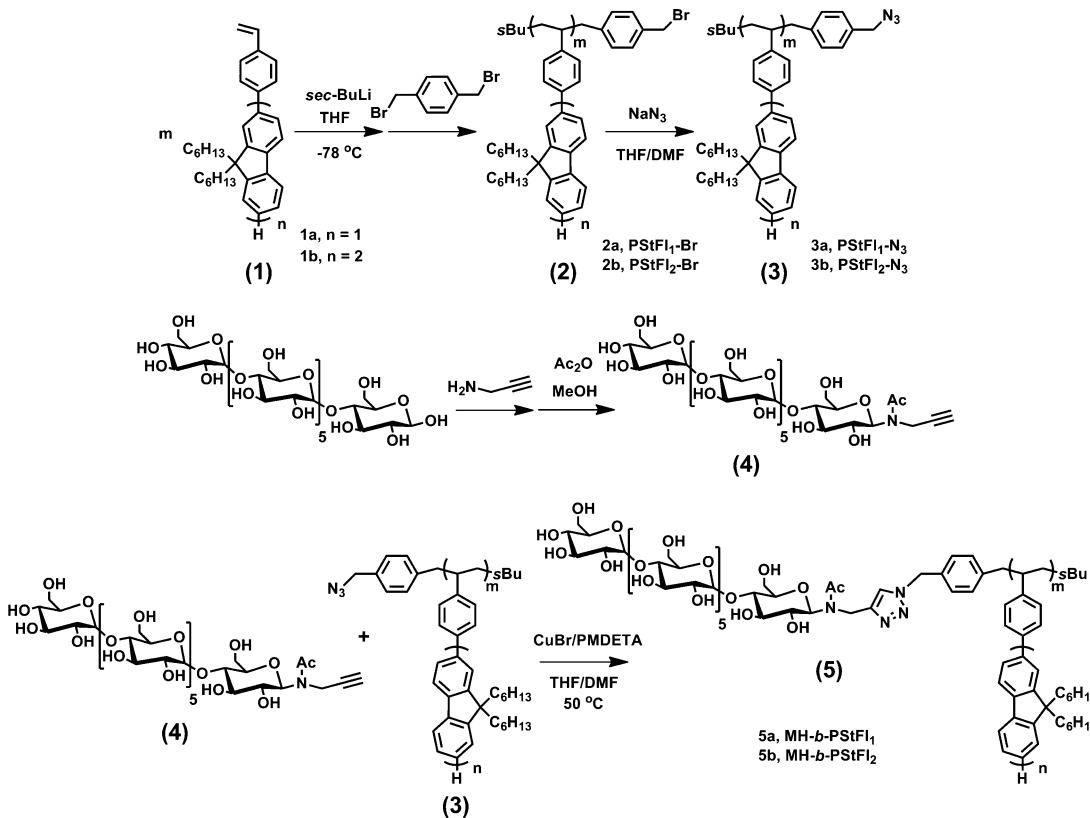
With the rapid development of electronic techniques, the requirement of memory devices dramatically increases. Organic

nonvolatile memory (ONVM) devices have been receiving significant research interest due to their advantageous merits of solution and low-temperature processability, mechanical flexibility, light weight, and low cost.³ Among the various ONVM devices, transistor type is the main one dominating the memory market because of its low-power-consumption reading feature, integrated circuit compatibility, and multibit storage capability.^{4,5} The transistor-type memory device is in principle rooted in a conventional transistor, while it has an additional charge storage layer sandwiched between the semiconductor and the dielectric layer which can be the ferroelectric materials,⁵ polymer electrets,⁶ or nanofloating gates.⁷ Among the aforementioned dielectric layers, polymer electrets have attracted extensive attention in recent years because they can readily stabilize trapped charges through their functional

Received: March 28, 2015

Revised: May 21, 2015

Published: June 3, 2015

Scheme 1. Synthetic Route for MH-*b*-PStFl_n (*n* = 1 or 2) Diblock Copolymers

groups.^{8,9a,9b} Recently, we found that the high performance of transistor memory devices could be achieved through the morphology manipulation (sphere, vertical or horizontal cylinder) of the oligosaccharide-based composite electret of maltoheptaose-*block*-polystyrene/1-aminopyrene.^{1d} As a remaining issue, the effects of the chemical structure of the oligosaccharide-based block copolymers on the transistor memory characteristics have not been fully explored yet. Moreover, the synthesis and self-assembling morphology of such block copolymers with electroactive moieties are still seldomly reported in the literature.

In this study, we report the synthesis and self-assembling morphology of the new oligosaccharide-based diblock copolymers, MH-*b*-PStFl_n (*n* = 1 or 2, Scheme 1), as polymer electrets for the organic field effect transistor (OFET) memory applications. PStFl_n containing oligofluorenyl side chains are electroactive polymers, which significantly differ from the previously reported nonconjugated polystyrene block.¹² The self-assembling structures of the MH-*b*-PStFl_n diblock copolymers were investigated by the transmission electron microscopy (TEM), atomic force microscopy (AFM), small-angle X-ray scattering (SAXS), and grazing-incidence small-angle scattering (GISAXS). The MH-*b*-PStFl_n electret-based OFET memory devices using p-type pentacene as a charge transport layer were fabricated into a bottom-gate/top-contact configuration. The effects of conjugation length of the PStFl_n side chain on the morphology and OFET memory characteristics were investigated throughout this study.

EXPERIMENTAL SECTION

Materials. The following chemicals were used as received, including 2-bromofluorene (95%, Aldrich), 1-bromohexane (98%, Aldrich), 9,9-dihexyl-2,7-dibromofluorene (97%, Aldrich), triisopropyl

borate (>98%, Aldrich), tetrakis(triphenylphosphine)palladium(0) (Pd(PPh₃)₄, 99%, Aldrich), acetic anhydride (>98.0%, Aldrich), sodium azide (>99.5%, Aldrich), propargylamine (>95.0%, TCI), sodium hydroxide (>98%, Aldrich), sodium carbonate (99.6%, Acros), 4-bromostyrene (98%, Aldrich), *n*-butyllithium (*n*-BuLi, 2.5 M in hexane, Chemetall), sec-butyllithium (sec-BuLi, 1.3 M in cyclohexane/hexane (92/8), Chemetall), Aliquat 336 (triethylmethylammonium chloride, Aldrich), hydrochloric acid (HCl, 37%, Aldrich), methyl sulfoxide (>99.9%, Acros), toluene (anhydrous, Acros), methanol (>99%, Aldrich), chloroform (Mallinckrodt Chemical, Inc.), *N,N*-dimethylformamide (>99%, Acros), tetrahydrofuran (99.9%, Acros), phosphorus pentoxide (>98.0%, Aldrich), sulfuric acid (98.0%, Aldrich), sodium bicarbonate (>99.7%, Aldrich), lithium aluminum hydride (95%, Aldrich), heptane (99%, Aldrich), *tert*-butylbenzene (99%, Aldrich), sodium (99.9%, Aldrich), and naphthalene (99%, Aldrich). Tetrahydrofuran (THF) was refluxed over sodium wire, distilled over LiAlH₄ under nitrogen, and then distilled from its sodium naphthalenide solution under high-vacuum conditions (10⁻⁶ Torr). Heptane and *tert*-butylbenzene were washed with concentrated H₂SO₄, water, and aqueous NaHCO₃, dried over P₂O₅, and finally distilled in the presence of 1,1-diphenylethylene with standardized octanol in THF solution under high-vacuum conditions. Maltoheptaose (MH) was purchased from Hayashibara Biochemical Lab (Japan). Sublimed pentacene was purchased from Luminescence Technology Corp. (Taiwan). StFl₁ and StFl₂ monomers and their corresponding bromo-terminated homopolymers were prepared according to our previous work.⁹ The ethynyl-terminated maltoheptaose was prepared according to the reported method.¹⁰

Synthesis of Azido-Terminated PStFl_n Homopolymers (PStFl_n-N₃, 3 (*n* = 1 or 2)). As a typical method, the bromo-terminated PStFl₁ (250 mg, 0.025 mmol, *M*_{n,NMR} = 10 300 g/mol) was dissolved in THF (2.5 mL), followed by adding excess NaN₃ (8.13 mg, 0.125 mmol) in DMF (2 mL). The reaction mixture was stirred for 72

h at room temperature. The reaction solution was passed through a basic alumina column to remove the remaining NaN_3 and salts. The polymer was reprecipitated twice in methanol and then dried in a vacuum to afford $\text{PStFl}_1\text{-N}_3$ as a light yellow solid (237 mg, 95% yield). ^1H NMR (400 MHz, CDCl_3 , δ (ppm)): 7.7–6.4 (broad, aromatic protons), 2.7–1.1 and 1.1–0.3 (broad, polymer backbone and $-\text{C}_6\text{H}_{13}$). IR (KBr): 2095 cm^{-1} ($-\text{N}_3$ stretching). $M_{n,\text{GPC}} = 7020$ g/mol, $M_w/M_n = 1.08$. The $\text{PStFl}_2\text{-N}_3$ ($M_{n,\text{NMR}} = 10\,260$ g/mol) was prepared under the same reaction conditions. $\text{PStFl}_2\text{-N}_3$: ^1H NMR (400 MHz, CDCl_3 , δ (ppm)): 7.8–6.4 (broad, aromatic protons), 2.7–1.2 and 1.2–0.3 (broad, polymer backbone and $-\text{C}_6\text{H}_{13}$). IR (KBr): 2098 cm^{-1} ($-\text{N}_3$ stretching). $M_{n,\text{GPC}} = 7170$ g/mol, $M_w/M_n = 1.04$.

Synthesis of MH-*b*-PStFl_n (5) via Click Reaction. As a typical method, $\text{PStFl}_1\text{-N}_3$ (100 mg, 0.01 mmol, $M_{n,\text{NMR}} = 10\,300$ g/mol), the ethynyl-terminated maltoheptaose (24.64 mg, 0.02 mmol), and CuBr (2.87 mg, 0.02 mmol) were placed in a Schlenk flask. The flask was evacuated overnight and then backfilled with argon. Dry THF (2 mL) and DMF (2 mL) were sequentially added to dissolve $\text{PStFl}_1\text{-N}_3$ and the ethynyl-terminated maltoheptaose. PMDETA (6.93 mg, 0.04 mmol) was then slowly introduced. The reaction mixture was stirred vigorously for 72 h at 50 °C and monitored by FTIR measurements until the signal of azido group completely vanished. The polymer solution was purified over a short pad of silica gel to remove the copper complex. After the evaporation of solvent, the residue was precipitated in cold methanol several times to remove the excessive ethynyl-terminated maltoheptaose. The final product of MH-*b*-PStFl₁ was obtained as a yellowish solid (95 mg, 85% yield). ^1H NMR (400 MHz, $\text{CDCl}_3/\text{DMSO}-d_6$, δ (ppm)): 7.9–6.3 (broad, aromatic protons), 5.7–3.3 (protons from maltoheptaose moiety), 2.7–1.1 and 1.1–0.1 (broad, polymer backbone, acetyl and $-\text{C}_6\text{H}_{13}$). $M_{n,\text{GPC}} = 7280$ g/mol, $M_w/M_n = 1.09$. Anal. Calcd for $\text{C}_{818}\text{H}_{1014}\text{N}_4\text{O}_{36}$: C 85.58%, H 8.90%, N 0.49%. Found: C 85.70%, H 8.43%, N 0.40%. The MH-*b*-PStFl₂ block copolymer was synthesized by the similar procedures. MH-*b*-PStFl₂: ^1H NMR (400 MHz, $\text{CDCl}_3/\text{DMSO}-d_6$, δ (ppm)): 7.9–6.4 (broad, aromatic protons), 5.7–3.3 (protons from maltoheptaose moiety), 2.3–1.1 and 1.1–0.2 (broad, polymer backbone, acetyl and $-\text{C}_6\text{H}_{13}$). $M_{n,\text{GPC}} = 7320$ g/mol, $M_w/M_n = 1.06$. Anal. Calcd for $\text{C}_{813}\text{H}_{1030}\text{N}_4\text{O}_{36}$: C 85.39%, H 9.08%, N 0.49%. Found: C 85.47%, H 8.83%, N 0.48%.

Sample Preparation for Morphological Analysis. As a typical procedure, MH-*b*-PStFl₁ (or MH-*b*-PStFl₂) was first dried in a vacuum oven at room temperature for 1 day and dissolved in toluene or chloroform to form a 10 mg/mL polymer solution. The bulk samples were prepared by placing the polymer solutions (chloroform) in 1 mL Teflon beakers and sequentially evaporating the solvent slowly at room temperature for several days. Thereafter, the bulk samples were further dried and annealed in a vacuum at 180 °C for 72 h.

Polymer thin films were prepared by spin-coating the polymer solutions (toluene as solvent) onto 100 nm SiO_2 -coated silicon wafers at a spinning rate of 2000 rpm for 60 s. Film thickness was measured using a Filmetrics F20 interferometer or a Surfcoorder ET3000 profilometer (Kosaka Lab). The thickness of all polymer thin films was controlled around 50 nm. Thin films were then thermo-treated at 90 °C for 2 h or solvent-annealed at room temperature for 18 h by placing them into a tightly capped 2 L glass bottle, in which an uncapped 20 mL beaker containing a THF/water (2.0 g/2.0 g) mixture solvent was used.^{2b} After annealing, the polymer thin film was dried under vacuum overnight to remove the residue solvents.

Fabrication of Pentacene-Based OFET Memory Devices. The highly doped n-type silicon wafer was used as the substrate. A 100 nm thick SiO_2 layer as a gate dielectric was thermally grown onto the silicon substrates. The substrate was precleaned by an ultrasonic cleaning process with toluene, acetone, and isopropyl alcohol successively for 20 min each and dried with a steam of nitrogen. The polymer solution (in toluene, 10 mg/mL) was filtered through a PTFE membrane syringe filter with pore size of 0.22 μm and spin-coated onto the wafer substrate at 2000 rpm for 60 s. After that, the polymer thin film was dried under vacuum (10^{-7} Torr) at 90 °C for 1 h to remove residue solvents. The thickness of the obtained polymer

film was around 50 nm. The 50 nm thick pentacene film was thermally deposited at a deposition rate of 0.4–0.5 nm s^{-1} and a substrate temperature of 90 °C under vacuum (10^{-7} Torr). The 70 nm thick gold source and drain electrodes were subsequently deposited by thermal deposition through a regular shadow mask. The channel length (L) and width (W) were 50 and 1000 μm , respectively. The current–voltage characteristics of the devices were measured by using a Keithley 4200-SCS semiconductor parameter analyzer in a N_2 -filled glovebox.

Characterization. The molecular weight ($M_{n,\text{GPC}}$) and molecular weight distribution (M_w/M_n) of the prepared polymer were determined by the gel permeation chromatography (GPC) using a Lab Alliance RI2000 instrument equipped with Waters Styragel HR2 and HR4 THF 7.8 \times 300 mm columns and a refractive index detector. THF was used as the eluent solvent at a flow rate of 1 mL/min at 40 °C. $M_{n,\text{GPC}}$ and M_w/M_n were calculated on the basis of a polystyrene calibration. The ^1H NMR measurements were carried out using a Bruker Avance DRX 400 MHz FT-NMR system. FT-IR spectra were recorded at room temperature using a PerkinElmer 100 Model FT-IR spectrophotometer. Samples were cast on KBr pellets and scanned 16 times at a resolution of 4 cm^{-1} . The CHN elemental analysis was performed using the “elemental Vario EL cube” elemental analyzer (for NCSH, German). Thermogravimetric analysis (TGA) was performed on a TA Q50 TGA. 3–5 mg powder samples were heated under flowing nitrogen (flow rate 100 cm^3/min) at a heating rate of 10 °C/min from room temperature to 800 °C. The glass transition temperatures (T_g) were determined using a TA Instruments DSC Q100 at a heating rate of 5 °C/min from –30 to 250 °C.

The UV–vis absorption spectrum was recorded on a Hitachi U-4100 spectrophotometer. For the thin film spectra, polymers were first dissolved in toluene (10 mg/mL), followed by filtering through a PTFE membrane syringe filter with pore size of 0.22 μm , and then spin-coated onto a quartz substrate at a spinning rate of 2000 rpm for 60 s. Cyclic voltammetry (CV) was performed on a CHI 611D electrochemical analyzer using a three-electrode cell in which ITO (polymer films area were about 0.5 \times 0.7 cm^2) was used as a working electrode. A platinum wire was used as an auxiliary electrode. All cell potentials were obtained with the use of a homemade Ag/AgCl, KCl(sat.) reference electrode. The electrochemical properties of the polymer films were measured in 0.1 M dry acetonitrile solution containing tetra-*n*-butylammonium perchlorate as the electrolyte.

Samples for transmission electron microscopy (TEM) measurements were prepared by embedding the thermo-annealed bulk block copolymer samples in epoxy resin, cured at 60 °C overnight, and microtomed to sections with thickness ~80 nm. To enhance the contrast, the thin film was exposed to RuO_4 vapor that selectively stains the PStFl₁ or PStFl₂ block. TEM images were collected on a Joel JEM-1230 transmission electron microscope at an accelerating voltage of 100 kV. Atomic force microscopy (AFM) imaging was performed on a MultiMode AFM system with a Nanoscope 3D controller (Digital Instruments) in a tapping mode. The spring constant of the silicon cantilevers (Nanosensor PPP-SEIHR) was 15 N/m, and the resonant frequency was 130 kHz. The thickness of polymer film was measured with a Microfigure Measuring Instrument (Surfcoorder ET3000, Kosaka Laboratory Ltd.) or a Filmetrics F20 interferometer. The small-angle X-ray scattering (SAXS) measurements were performed on beamline BL 23A1 in the National Synchrotron Radiation Research Center (NSRRC), Taiwan. A monochromatic beam of $\lambda = 0.887 \text{ \AA}$ (15 keV) was used.¹¹ SAXS spectra were collected on a Pilatus 1 M detector with an area of 169 mm \times 179 mm (981 pixels \times 1043 pixels). The 1-D scattering intensity profiles were obtained by circularly averaging the 2-D pattern and reported as the plots of scattering intensity I versus the scattering vector q , where $q = (4\pi/\lambda) \sin(\theta/2)$, λ is the wavelength of incident X-rays, and θ is the scattering angle. Grazing incidence small-angle X-ray scattering (GISAXS) data were also collected on beamline BL23A1 in NSRRC, with a wavelength of 0.827 \AA (15 keV) at an incident angle of 0.15°. The samples were prepared on 1.8 cm \times 2.4 cm Si substrates. The capacitance of the bilayer dielectrics was measured on the MIS structure using Keithley 4200-SCS equipped with a digital capacitance meter (model 4210-CVU).

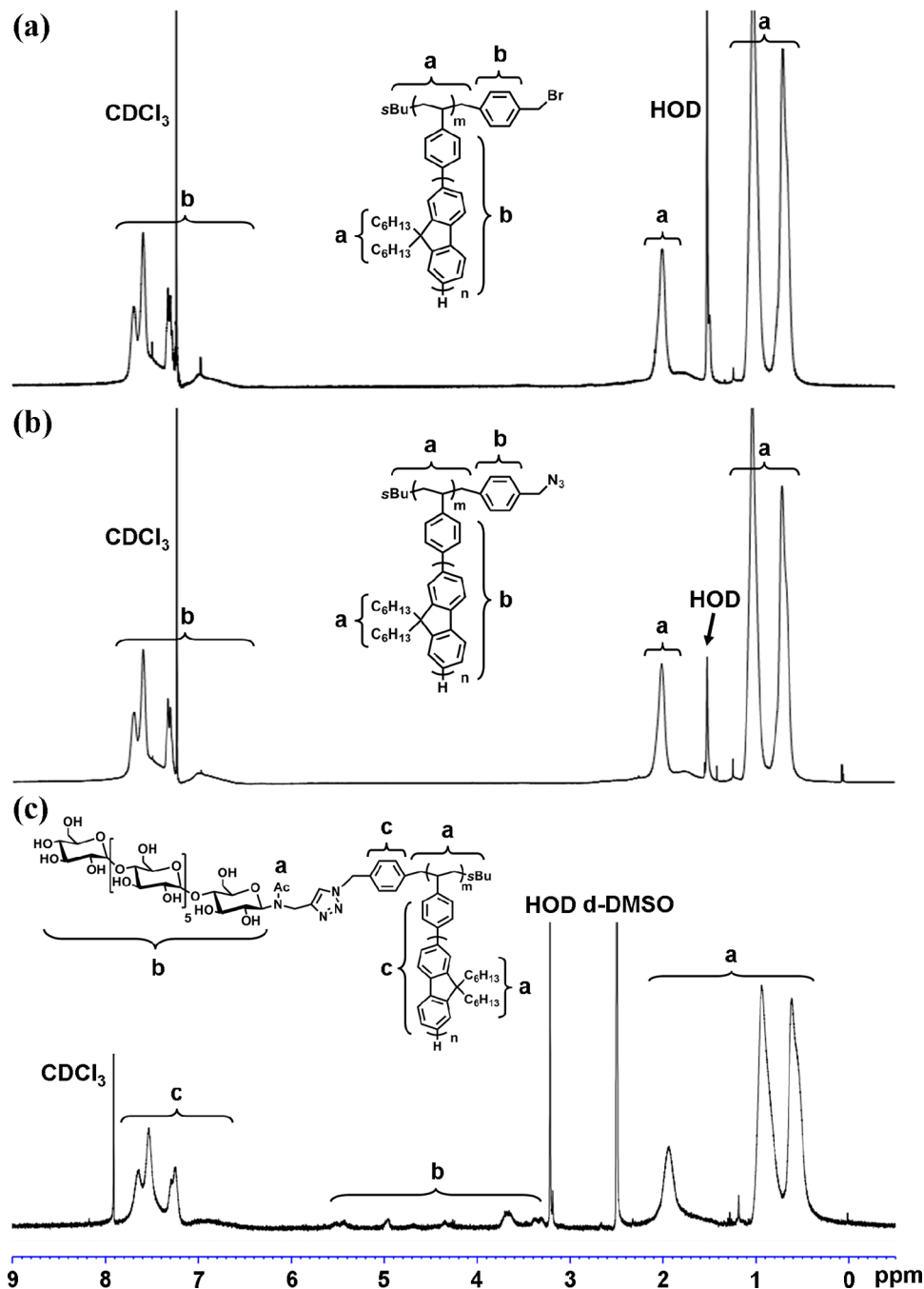


Figure 1. ¹H NMR spectra of (a) bromo-terminated PStFl₂ in CDCl₃, (b) azido-terminated PStFl₂ in CDCl₃, and (c) MH-*b*-PStFl₂ diblock copolymer in CDCl₃/DMSO-*d*₆.

Computational Methodology. Theoretical molecular simulation of the oligofluorene moieties (StFl₁ and StFl₂) were calculated through the Gaussian 03 program package.¹² The density functional theory (DFT) method, using Becke's three-parameter functional with the Lee, Yang, and Parr correlation functional method (B3LYP) with 6-31G, was exploited for the optimization of ground-state molecular geometry.

RESULTS AND DISCUSSION

Chemical Structure Characterization. The azido-terminated PStFl_ns (PStFl_n-N₃s, *n* = 1 or 2) were prepared by reacting the previously reported bromo-terminated PStFl_ns (PStFl_n-Br)s⁹ with NaN₃ in THF/DMF, and the MH-*b*-PStFl_ns were obtained from the click reactions of PStFl_n-N₃s with

excess ethynyl-terminated maltoheptose (MH). The chemical structures of PStFl_n-Br, PStFl_n-N₃, and MH-*b*-PStFl_n were confirmed by ¹H NMR and FT-IR measurements. The ¹H NMR spectra of PStFl_n-Br are in good agreement with those in the reported literature,⁹ as shown in Figure 1a and Figure S2 (Supporting Information). The proton signals belonging to both main and side chains are clearly observed in the regions of 7.7–6.4, 2.7–1.1, and 1.1–0.3 ppm due to the aromatic protons, main chain backbone, and alkyl side chain, respectively. After the electrophilic substitution of the end Br to azido group, a shift of the -CH₂Br (proton peak) was examined. Unfortunately, both of the proton signals from -CH₂Br and -CH₂N₃ are not observed in the ¹H NMR

spectra probably due to the low signal-to-noise ratio (Figure 1a,b and Figure S2). The N_3 group at the PStFl_n end is however verified by the FT-IR measurements as its characteristic stretching absorption at 2098 cm^{-1} clearly appeared after the azidation reaction, as shown in Figure 2 and Figure S3. After

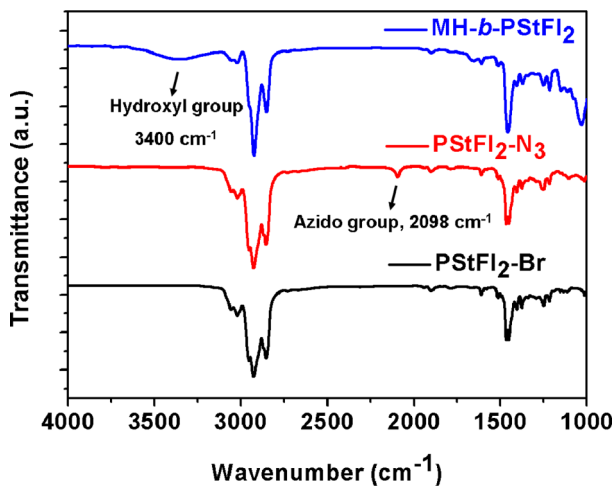


Figure 2. FT-IR spectra of bromo-terminated PStFl₂, azido-terminated PStFl₂, and MH-*b*-PStFl₂ diblock copolymer.

click reaction of each PStFl_n-N₃ with the ethynyl-terminated MH, the characteristic proton signals from MH block are distinctly observed in the region of 3.3–5.7 ppm (Figure S1) though they appear at slighter upfield in comparison to the normal situation in a polar deuterated solvent,¹⁰ due to the aggregation effect of MH segments in CDCl₃/DMSO-*d*₆, as shown in Figure 1c and Figure S2. The simultaneous appearance of the proton signals of MH and PStFl_n blocks in the ¹H NMR spectra strongly suggests that MH-*b*-PStFl_n is successfully prepared. This inference is further evidenced by the FT-IR measurements and elemental analyses; i.e., after click reaction, the peak at 2098 cm^{-1} due to the N₃ in PStFl_n-N₃ disappeared completely, and the new absorption around 3400 cm^{-1} due to hydroxyl groups of MH is clearly observed; the elemental analysis of the block copolymers indicated that the compositions of the diblock copolymers were rather close to the theoretical values.

The molecular weight ($M_{n,\text{GPC}}$) and molecular weight distribution (M_w/M_n) of PStFl_n-N₃ were estimated by ¹H NMR and GPC measurements, as listed in Table 1. All the GPC measurements of PStFl_n-N₃s in Figure S4 under the monodispersed GPC traces, from which the estimated $M_{n,\text{GPC}}$ s show a deviation from their corresponding theoretical ones due to the structural inconsistency between the PStFl_n-N₃ and polystyrene standard. The obtained M_w/M_n values of PStFl_n-N₃s are extremely low as 1.04–1.08. Comparing with the $M_{n,\text{GPC}}$ s, the molecular weights ($M_{n,\text{NMR}}$) estimated from ¹H NMR measurements are much more accurate because each $M_{n,\text{NMR}}$ of PStFl_n-N₃ matches well with its targeted value around 10K g/mol, as desired. The click reactions of PStFl_n-N₃s with the excessive ethynyl-terminated MH (MW = 1232 g/mol) were carried out to prepare MH-*b*-PStFl_ns, after which the unreacted ethynyl-terminated MH was removed by reprecipitating MH-*b*-PStFl_n into methanol. Each click reaction is verified by the shifting of GPC trace toward the high molecular weight region after block copolymer synthesis, as shown in Figure S4. Meanwhile, all the obtained MH-*b*-PStFl_n values

Table 1. Syntheses and Physical Properties of PStFl_n Homopolymers and MH-*b*-PStFl_n (*n* = 1 or 2) Diblock Copolymers

sample	$M_{n,\text{NMR}}$ (g/mol)	$M_{n,\text{GPC}}^c$ (g/mol)	M_w/M_n^c	T_d^d (°C)	T_g^e (°C)	<i>d</i> -spacing ^f (nm)
PStFl ₁ -N ₃ ^a	10300	7020	1.08	328	87	n.a. ^g
PStFl ₂ -N ₃ ^a	10260	7170	1.04	378	88	n.a. ^g
MH- <i>b</i> -PStFl ₁ ^b	11530	7280	1.09	292	91	9.2
MH- <i>b</i> -PStFl ₂ ^b	11490	7320	1.06	263	91	7.7

^aEstimated by ¹H NMR in CDCl₃. The number-average molecular weight of PStFl_n-N₃ was calculated by using the following formula: $M_{n,\text{NMR}}(\text{PStFl}_n) = [\text{fluorene monomer}]_0/[\text{initiator}]_0 \times (\text{MW of fluorene monomer}) \times \text{Conv} + (\text{MW of initiator}) + (\text{MW of end-capped reagent})$. ^bEstimated by ¹H NMR in CDCl₃/d-DMSO and result of element analysis. ^cMeasured by GPC using PSt standards in THF. ^dOnset weight loss temperature determined by TGA at a heating rate of 10 °C/min under a N₂ atmosphere. ^eDetermined by DSC with 5 °C/min heating rate under a N₂ atmosphere. ^fDetermined by SAXS measurement using thermal-annealed bulk samples. ^gNot available.

have rather low M_w/M_n values at 1.06–1.09, similar to those of their precursors, PStFl_n-N₃.

Thermal Property Analyses. The thermal properties of MH, PStFl_n-N₃, and MH-*b*-PStFl_n were measured by TGA and DSC, as shown in Figure 3 and Figure S5. Table 1 summarizes all the thermal decomposition temperatures (T_d , onset weight loss temperature) and glass transition temperatures (T_g). As

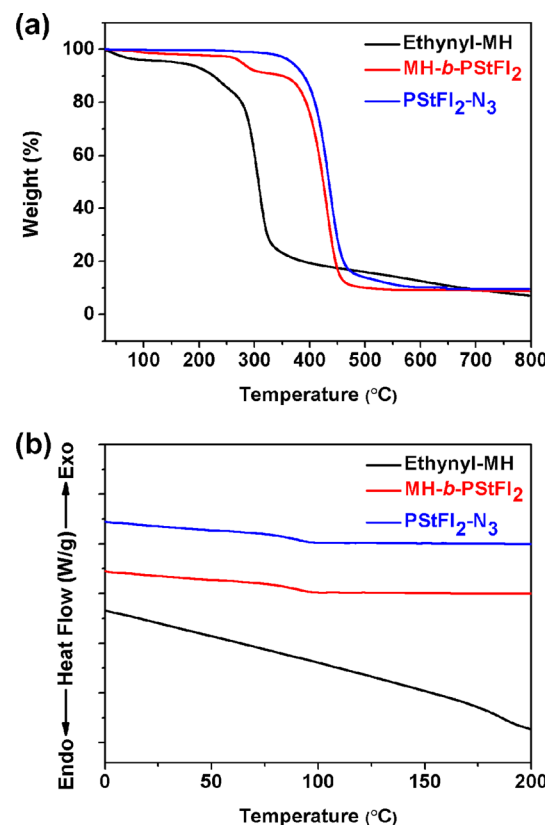


Figure 3. (a) TGA diagrams and (b) DSC curves of the ethynyl-terminated MH, PStFl₂-N₃, and MH-*b*-PStFl₂ diblock copolymer.

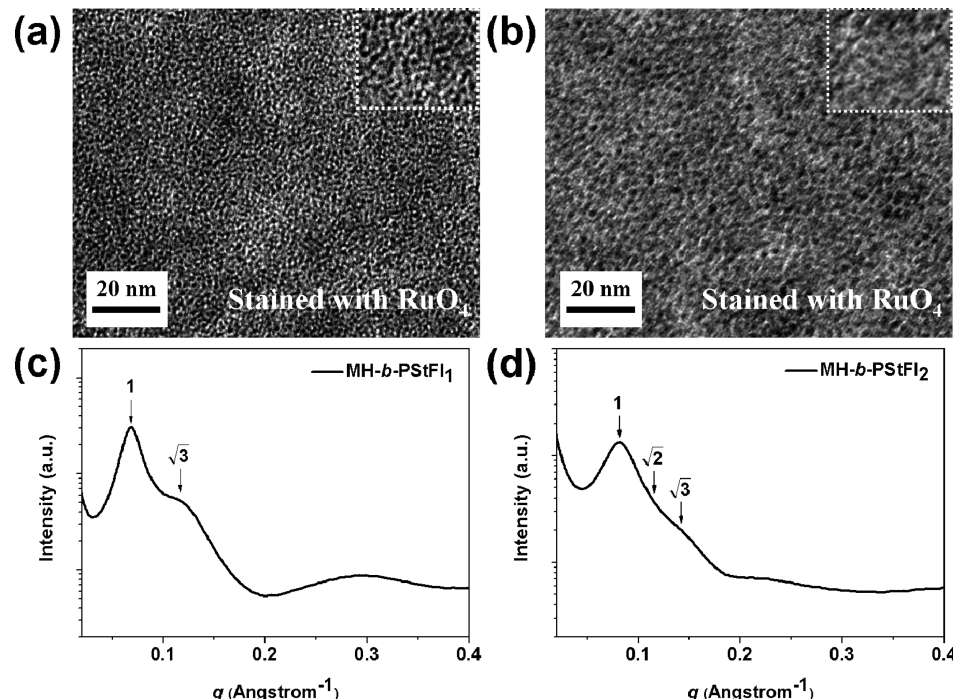


Figure 4. TEM images of MH-*b*-PStFl_{*n*} (*n* = 1 or 2) diblock copolymers: (a) MH-*b*-PStFl₁ and (b) MH-*b*-PStFl₂. SAXS data of MH-*b*-PStFl_{*n*} diblock copolymer: (c) MH-*b*-PStFl₁ and (d) MH-*b*-PStFl₂.

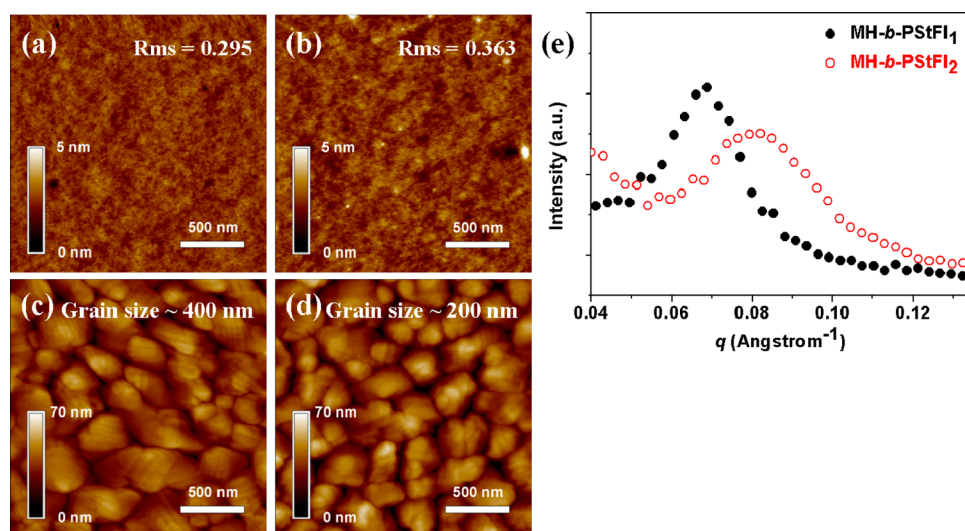


Figure 5. Surface structures of the thermal-annealed MH-*b*-PStFl_{*n*} (*n* = 1 or 2) thin film (electret layer) and pentacene layer grown on the thermal-annealed MH-*b*-PStFl_{*n*} film: MH-*b*-PStFl₁ was used for (a) and (c); MH-*b*-PStFl₂ was used for (b) and (d). (e) 1-D GISAXS q_y scan plots at $q_z = 0.027$ Å⁻¹ of MH-*b*-PStFl₁ and MH-*b*-PStFl₂ thin films.

shown in Figure 3a for MH, an obvious weight loss prior to 100 °C is observed, which could be attributed to the evaporation of the adsorbed moisture by MH. MH and PStFl_{*n*}-N₃ have the T_d values around 207 and 328–383 °C, respectively. The T_d of PStFl_{*n*}-N₃ is enhanced with increasing either the conjugation length of the oligofluorenyl unit or molecular weight, or both, since increasing aromatic ingredient and/or molecular weight generally increases the T_d . The MH-*b*-PStFl_{*n*} exhibits a two-stage thermal degradation separately locating in the regions of 260–310 and 400–450 °C, which correspond to the decomposition of MH and PStFl_{*n*} blocks, respectively. Notably, the T_d values of MH-*b*-PStFl_{*n*}s are much lower than their corresponding PStFl_{*n*}-N₃ homopolymers due to the low

thermal stability of the MH segment. Similarly to PStFl_{*n*}-N₃, MH-*b*-PStFl_{*n*} with a longer oligofluorenyl side chain shows a higher T_d at the second degradation; i.e., the T_d at the second degradation of MH-*b*-PStFl₂ is much higher than that of MH-*b*-PStFl₁. No endothermic peak due to T_g is observed for MH on its DSC curves of MH, PStFl_{*n*}-N₃, and MH-*b*-PStFl_{*n*} as shown in Figure 3b. The endothermic peak at 190 °C is considered to be related to the caramelization of MH, rather than T_g . The T_g s of both PStFl_{*n*}-N₃ and MH-*b*-PStFl_{*n*} are extremely similar to each other around 90 °C. Thus, the T_g of MH-*b*-PStFl_{*n*} is attributed to the PStFl_{*n*} block since MH does not show any T_g around this temperature.

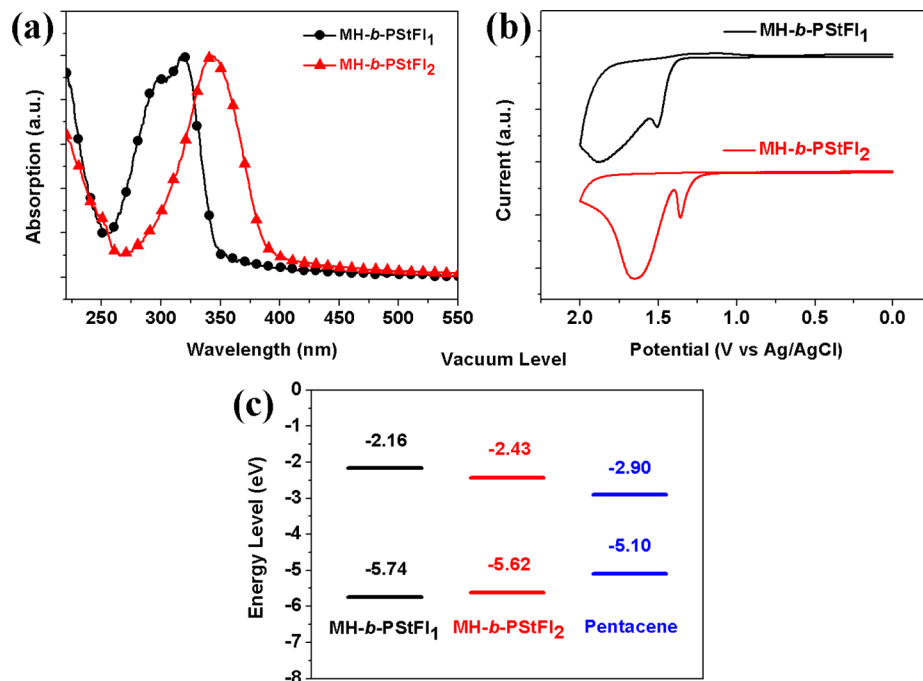


Figure 6. Optical absorption, electrochemical property, and energy level of MH-*b*-PStFl_{*n*} (*n* = 1 or 2) diblock copolymers: (a) UV-vis spectra, (b) cyclic voltammograms of MH-*b*-PStFl_{*n*} block copolymers thin films, and (c) energy level of MH-*b*-PStFl block copolymers and pentacene.

Morphology Characterization. Figures 4a and 4b show the transmission electron microscopy (TEM) images on the microtomed sections of the thermal-annealed MH-*b*-PStFl_{*n*} (*n* = 1 or 2) bulk sample, in which the dark part is assigned to the PStFl_{*n*} block stained with RuO₄ and the bright part to the MH block. Obviously, the MH block tends to self-assemble into spherical nanoaggregates with the domain size around 4–5 nm and uniform dispersion. Such nanoaggregates are also clearly observed in the AFM images, as shown in Figure 5a,b and Figure S6. The as-cast and thermo-treated MH-*b*-PStFl₁ films with small root-mean-square (RMS) roughness of 0.265–0.295 nm have a much smoother surface than that of MH-*b*-PStFl₂, whose RMS is around 0.319–0.363 nm. The higher roughness of the MH-*b*-PStFl₂ thin film is probably due to the greater stiffness and stronger molecular interaction of the PStFl₂ block, which causes the more irregular packing. After solvent annealing, both of the MH-*b*-PStFl₁ and MH-*b*-PStFl₂ thin films, with the RMS roughness of 0.277 and 0.265, respectively, have the smoother surfaces than the as-cast and thermal-annealed films, indicating that the solvent annealing process should have facilitated the polymer chain relaxation and ameliorated the arrangement of the polymer chains. In order to further investigate the self-assembling behavior of the block copolymers, we took insight into the ordering patterns of the thermal-annealed bulk MH-*b*-PStFl_{*n*} samples by the small-angle X-ray scattering (SAXS) technique. Figure 4c,d shows the SAXS profiles of thermal-annealed bulk samples. All the bulk samples prepared from MH-*b*-PStFl_{*n*} show the clear first-order scattering peaks, which are located at $q^* = 0.068$ and 0.082 \AA^{-1} for the MH-*b*-PStFl₁ and MH-*b*-PStFl₂ bulk samples, respectively. The *d*-spacing (center-to-center distance) is calculated accordingly based on the scattering formula of $d = 2\pi/q^*$, from which the *d* values are 9.2 and 7.7 nm for the corresponding bulk samples, respectively. The SAXS results are consistent with the calculated values on the degree of polymerization (DP), which are 23 and 13 for PStFl₁ and

PStFl₂ blocks, respectively. The *d*-spacing reasonably increases with the increase of chain length of PStFl_{*n*} segment. In addition to the first-order scattering peak, a higher-order peak, which follows the relationship of $\sqrt{3}$ comparing with the first-order peak as 1, is also observed. Theoretically, the appearance of this peak is attributed to either a body-centered cubic (BCC) or a cylindrical hexagonal packing pattern. We herein prefer the BCC sphere structure rather than the cylinder one, though the characteristic $\sqrt{2}$ peak for the BCC pattern is not clearly observed. Note that the high weight fraction of the PStFl_{*n*} block ($f_{\text{PStFl}_n} > 0.9$ by weight) more favorably leads to forming the spherical structures. The TEM images in Figure 4b complementarily support this hypothesis. Other higher-order scattering peaks are unapparent due to the lack of long-range ordering. Besides the 1 and $\sqrt{3}$ scattering peaks, an extra broad peak located in the region of high q^* is observed, which is assigned to the interlayer distance formed between the rigid oligofluorenyl moieties caused by the self-arrangement themselves. The q^* values of 0.294 and 0.231 \AA^{-1} corresponding to the interlayer spacing of 2.16 and 2.72 nm result from the pendent StFl₁ and StFl₂ moieties, respectively. Based on the results from the Gaussian theoretical calculation, the fully stretched molecular lengths of StFl₁ and StFl₂ are approximately 1.28 and 2.11 nm. The interlayer distance of 2.16 or 2.72 nm is much greater than its related molecular length of 1.28 or 2.11 nm but less than twice the length of the fully stretched StFl₁ or StFl₂ molecule. This indicates that the PStFl_{*n*} blocks in the separated layers are interlocked with each other between two adjacent layers.¹³

The molecular packing fashion of MH-*b*-PStFl_{*n*} in the thin films was further investigated by grazing incidence small-angle X-ray scattering (GISAXS). Figure S7 shows the 2-D GISAXS patterns, in which the diffraction spots only appeared along the q_y -axis. The plots of the q_y are scanned at $q_z = 0.027 \text{ \AA}^{-1}$, as shown in Figure S6 and Figure S8. The 1-D q_y scanning plots of the MH-*b*-PStFl₁ and MH-*b*-PStFl₂ thin films show the clear

first-order peaks, while no obvious higher-order peak is observed. Together considering the SAXS results of the bulk samples, we assume that they self-assemble to form the nanospherical structures. From the scattering vector of the primary reflection, the obtained *d*-spacing values are 9.2, 9.2, and 11.0 nm for the as-cast, thermal-treated, and solvent-annealed MH-*b*-PStFl₁ films and 7.9, 7.7, and 9.0 nm for MH-*b*-PStFl₂ films, respectively. The GISAXS results again support the formation of the BCC spherical structures which are self-organized by MH-*b*-PStFl_{*n*}. Notably, the stronger GISAXS intensity and narrower full width at half-maximum (fwhm) of the solvent-annealed thin films indicate that the solvent annealing process is indeed an efficient way to facilitate the MH-*b*-PStFl_{*n*} diblock copolymers to form the well-defined self-assembled nanostructures. The GISAXS results also demonstrate that the molecular packing of solvent-annealed MH-*b*-PStFl_{*n*} thin films is much better than those of the as-cast and thermal-treated thin films. In addition to the surface information on the MH-*b*-PStFl_{*n*} electrets, the AFM images of the pentacene layer after deposited on the polymer electrets are also shown in Figure 5 and Figure S9. The observation by AFM indicates that the granular structure of the pentacene crystal in its thin film, which is formed on the polymer electrets. The grain sizes of pentacene crystal grown from the MH-*b*-PStFl₁ and MH-*b*-PStFl₂ surfaces are 300–400 and 200–300 nm, respectively. The grain size obviously decreases with increasing the length of pendent oligofluorenyl unit. This might be due to the different torsion angles of StFl₁ and StFl₂; i.e., a small torsion angle of StFl₁ leads to more ordered packing fashion and gives a larger grain size, while the situation of StFl₂ is opposite.¹⁴

Optical and Electrochemical Properties. The optical and electrochemical properties of PStFl_{*n*}-N₃ and MH-*b*-PStFl_{*n*} were investigated by UV-vis and cyclic voltammogram (CV) measurements, as shown in Figure 6 and Figure S10 and summarized in Table 2. The optical band gaps (E_g^{opt}) of PStFl₁-

b-PStFl_{*n*}, the maximum and onset absorption wavelengths of the PStFl_{*n*}-based polymers show the red-shifting as compared with those of the PStFl₁-based polymers, obviously caused by the long conjugation length of StFl₂ moiety. The highest occupied molecular orbital (HOMO) energy levels of the polymer electrets were calculated from the onset of oxidation waves in CV curves with reference to ferrocene (4.8 eV), based on the equation of HOMO (eV) = $-e(E_{\text{onset}}^{\text{ox}} - E_{1/2}(\text{ferrocene}) + 4.8 \text{ eV})$, while the lowest unoccupied molecular orbital (LUMO) energy levels were estimated from the difference between the optical band gap and HOMO level. The obtained HOMO levels of PStFl₁-N₃, PStFl₂-N₃, MH-*b*-PStFl₁, and MH-*b*-PStFl₂ are −5.82, −5.64, −5.74, and −5.62 eV, respectively, and their LUMO levels are −2.26, −2.45, −2.16, and −2.43 eV, respectively. The similar energy levels between each PStFl_{*n*}-N₃ and its related MH-*b*-PStFl_{*n*} indicated that the MH block does not show a significant effect on the electrochemical reaction during oxidation and reduction processes, and all the redox behaviors are caused by the electroactive PStFl_{*n*} block. The level of HOMO increasing and LUMO decreasing with enhancing the oligofluorenyl chain length indicates that the PStFl_{*n*}-based polymers have better electron-donating and electron-accepting abilities.

OFET Memory Characterization. The memory characteristics of the prepared OFET memory devices using MH-*b*-PStFl_{*n*} as the charge storage (electret) layer were then investigated. All devices were fabricated to have the bottom-gate/top-contact configuration with p-type pentacene as charge transport layer and the self-organized MH-*b*-PStFl_{*n*} thin film as electret layer, as shown in Figure 7a. The devices exhibit a typical p-type accumulation mode with well-defined linear and saturation regions (Figure S11), from which the field-effect mobility (μ) could be obtained. The detailed OFET characteristics are summarized in Table S1. The μ of pentacene on the PStFl₁ or MH-*b*-PStFl₁/SiO₂ dielectric is 0.51–0.56 cm² V^{−1} s^{−1}, while that on PStFl₂ or MH-*b*-PStFl₂/SiO₂ is 0.21–0.28 cm² V^{−1} s^{−1}. The greater μ in the former case is related to the larger grain size and fewer boundaries of the pentacene crystals on MH-*b*-PStFl₁ layer. The initial threshold voltages (V_{TH}) of the devices range from −7 to −2 V, and the ON/OFF current ratios ($I_{\text{ON}}/I_{\text{OFF}}$) are at the level of 10⁷–10⁸. To examine the memory characteristics of the MH-*b*-PStFl_{*n*}-based devices, the devices are operated under applying gate voltage pulse to observe the shifts on the transfer curves, as shown in Figure 7b,c. Upon exerting a positive gate bias ($V_g = 50 \text{ V}$, $V_d = 0 \text{ V}$ for 2 s), the entire transfer curve shifts toward the positive direction, as referred to as the “writing” process. This shift leads to a high drain current (ON state) at $V_g = 0 \text{ V}$. On the other hand, the transfer curve shifts reversely to the negative direction referred to as the “erasing” process upon providing a reverse (negative) gate bias ($V_g = -50 \text{ V}$, $V_d = 0 \text{ V}$ for 2 s). The shifting interval on the transfer curve after applying a writing and subsequently an erasing gate bias is defined as the memory windows (ΔV_{TH}).

We initially investigate the memory characteristics of two pentacene-based OFET memory devices as the control experiments, as shown in Figures S12 and S13a,b. The device without polymer electret layer only has a negligible threshold voltage shift, as shown in Figure S12a. In contrast, the device with the PStFl₁-N₃ or PStFl₂-N₃ electret layer sandwiched exhibits a memory window of 33 or 37 V, respectively. It indicates that the V_{TH} shift is significantly originated from the PStFl_{*n*} electret layer. In addition, the PStFl₁- and PStFl₂-

Table 2. Optical and Electrochemical Characteristics of PStFl_{*n*}-N₃ Homopolymers and MH-*b*-PStFl_{*n*} Block Copolymers

sample	λ^{max} in film ^a (nm)	E_g^{opt} ^b (eV)	HOMO/ $E_{\text{onset}}^{\text{ox}}$ ^c (eV/V)	LUMO ^d (eV)
PStFl ₁ -N ₃	319	3.56	−5.82/1.50	−2.26
PStFl ₂ -N ₃	342	3.20	−5.64/1.32	−2.45
MH- <i>b</i> -PStFl ₁	320	3.57	−5.74/1.42	−2.16
MH- <i>b</i> -PStFl ₂	342	3.19	−5.62/1.30	−2.43

^aSpun-cast film from toluene solution onto a quartz substrate.

^bOptical energy band gap estimated from onset wavelength (λ^{onset} (nm)) of the optical absorption using the formula $E_g^{\text{opt}} = 1240/\lambda^{\text{onset}}$ (nm).

^cThe HOMO energy level was determined from the onset

oxidation potential ($E_{\text{onset}}^{\text{ox}}$) and estimated on the basis of the

reference energy level of ferrocene (4.8 eV). The relative formula is

HOMO (eV) = $-e(E_{\text{onset}}^{\text{ox}} - E_{1/2}(\text{ferrocene}) + 4.8 \text{ eV})$. ^dThe LUMO energy level was estimated by the equation LUMO (eV) = HOMO + E_g^{opt} .

N₃, PStFl₂-N₃, MH-*b*-PStFl₁, and MH-*b*-PStFl₂ estimated from their onset wavelength (λ^{onset}) of the absorption spectra are 3.56, 3.20, 3.57, and 3.19 eV, respectively. The E_g^{opt} of each PStFl_{*n*}-N₃ is almost the same as that of its corresponding MH-*b*-PStFl_{*n*}, implying that the incorporation of MH to PStFl_{*n*} block has no significant effect on the electronic characteristics of PStFl_{*n*} block. No matter in which case of PStFl₁-N₃ and MH-

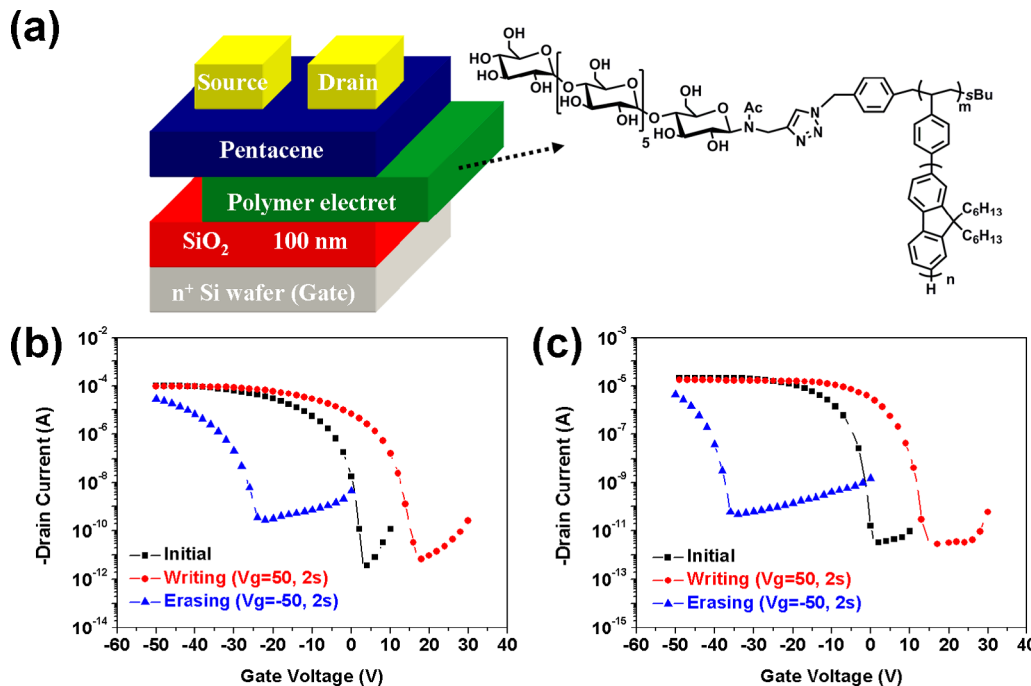


Figure 7. (a) Configuration of a transistor memory device and electric transfer curves of the memory devices using thermal-annealed MH-*b*-PStFl_n (*n* = 1 or 2) electrets: (b) MH-*b*-PStFl₁ and (c) MH-*b*-PStFl₂.

based memory devices have a much greater erasing V_{TH} s of -30 and -41 V than their writing V_{TH} s of 3 and -4 V. The large negative V_{TH} shift indicates that the StFl₁ and StFl₂ moieties prefers to trap the hole carriers. The PStFl₂-based device displays larger memory windows than the PStFl₁-based one, which suggests that a long conjugated length enhanced the charge storage ability. Apart from the control devices, the memory characteristics of the devices using MH-*b*-PStFl_n polymer electret are shown in Table 3 and Figure 7b,c. The

increased V_{TH} shift (10 V) in the positive direction after programming. In addition to the thermal treatment of the polymer electret layer, we also investigate the effect of solvent annealing process on the memory behavior of the MH-*b*-PStFl_n-based devices. Intriguingly, the devices using solvent-annealed MH-*b*-PStFl_n electrets have smaller positive V_{TH} shifts (4–5 V) after programming (Figure S13) when compared to the devices using the thermal-annealed MH-*b*-PStFl_n as electrets. The reason for this result is probably attributed to the improved arrangement of StFl_n moieties after solvent annealing since the solvent annealing process much prefer to induce polymer chain relaxation and afford more well-defined self-assembling structure, as supported by GISAXS results. In the present case, the electron-trapping MH block is possibly embedded in the StFl_n moiety, which forms a large electron injection barrier and thus reduces the charge trapping ability of the MH blocks. The mechanism for charge storage in MH-*b*-PStFl_n-based memory device is proposed as follows. On one hand, upon providing a positive gate pulse (the writing process) a large amount of negative charges are induced through pentacene from the source/drain electrode and eventually trapped within the polarized hydroxyl groups¹⁵ of the MH blocks in MH-*b*-PStFl_n electret, resulting in the positive shift of V_{TH} and a high-conductance state (ON state) at $V_g = 0$ V. In addition, the p-type nature of PStFl_n within nanoscale thin films serves as the tunneling layer. It enhances the built-in electric field^{15b,16} and prevents the leakage of the induced electrons even after removing the external gate voltage, which strengthens the retention characteristics. On the other hand, upon applying a negative gate pulse (erasing process), the transfer curve shifts toward the negative direction, which means that the trapped electrons are released or recombined by the holes that are injected from the pentacene layer to MH-*b*-PStFl_n electret; the device therefore returns to a low-conductance state (OFF state) at the $V_g = 0$ V. Importantly, the induced holes can easily transfer from pentacene layer to

Table 3. OFET Memory Characteristics of the Memory Devices Using PStFl_n-N₃ or MH-*b*-PStFl_n as the Polymer Electret

sample	μ^a (cm ² /(V s))	V_{TH}^b (V)	$V_{TH,writing}$ (V)	$V_{TH,erasing}$ (V)	ΔV_{TH}^c
PStFl ₁ -N ₃ ^d	0.56	-3	3	-30	33
PStFl ₂ -N ₃ ^d	0.21	-7	-4	-41	37
MH- <i>b</i> -PStFl ₁ ^d	0.51	-2	10	-30	40
MH- <i>b</i> -PStFl ₂ ^d	0.25	-3	9	-40	49
MH- <i>b</i> -PStFl ₁ ^e	0.52	-3	4	-33	37
MH- <i>b</i> -PStFl ₂ ^e	0.28	-2	5	-37	42

^aMobility calculated from saturation region and calibrated with the capacitance of polymer electrets. ^bThreshold voltage. ^c ΔV_{TH} is defined as $V_{TH,erasing} - V_{TH,writing}$. ^dThermal-annealed thin films. ^eSolvent-annealed thin films.

MH-*b*-PStFl₁- and MH-*b*-PStFl₂-based devices exhibit large erasing V_{TH} s of -30 and -40 V, respectively, which are extremely close to those of the above PStFl₁- and PStFl₂-based devices. The ΔV_{TH} s of the above two devices are 40 and 49 V, respectively, which are larger than those of the PStFl₁- ($\Delta V_{TH} = 33$ V) and PStFl₂-based ($\Delta V_{TH} = 37$ V) devices. The increase in memory windows could be reasonably attributed to the well-ordered arrangement of PStFl_n blocks after incorporating MH to the PStFl_n block. The abundant polar hydroxyl groups in the MH block play a role of electron trappers and thus result in the

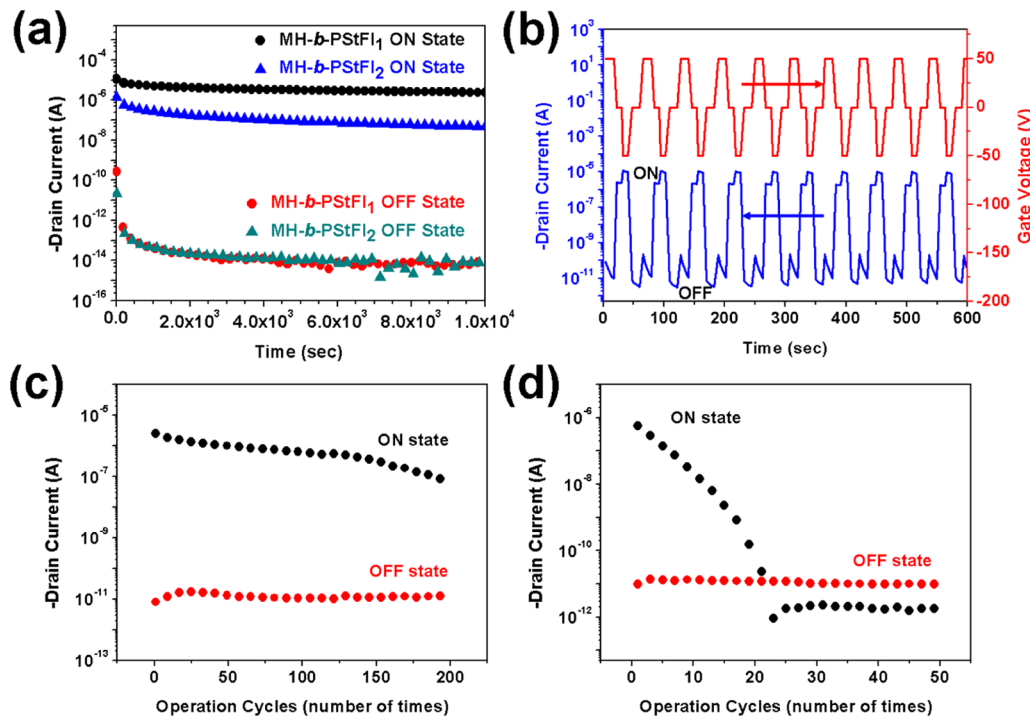


Figure 8. Memory characteristics of the memory devices using thermal-annealed MH-*b*-PStFl_{*n*} (*n* = 1 or 2) electret: (a) the retention time curves, (b) the write–read–erase–read (WRER) cycles for thermo-treated MH-*b*-PStFl₁ electret-based memory device and the operation cycles, (c) the switching stability of the MH-*b*-PStFl₁-based memory device, and (d) the switching stability of the MH-*b*-PStFl₂-based memory device.

the polymer electret layer because the HOMO energy barrier between pentacene (−5.10 eV) and PStFl_{*n*} matrix is small. Memory window slightly increases with increasing the conjugation length of the pendent oligofluorene moiety. This can be explained by the fact that the HOMO of PStFl₂ segment is smaller than PStFl₁, which makes holes inject into PStFl₂ more easily.

Figure 8a shows the retention time of the MH-*b*-PStFl_{*n*}-based OFET memory devices. The retention time of the ON and OFF states of the device at $V_g = 0$ V is maintained for 10^4 s with the $I_{\text{ON}}/I_{\text{OFF}}$ ratios at the level of 10^6 – 10^8 . This long retention time leads us to believe that the MH-*b*-PStFl_{*n*}-based OFET memory device is promising for organic nonvolatile memory applications. The ON/OFF switching stability of these devices was further evaluated based on write–read–erase–read (WRER) cycle measurements, as shown in Figure 8b–d. The WRER cycles were carried out as follows: the drain current was kept at $V_d = -30$ V, and the writing, reading, and erasing processes were implemented at $V_g = -50$, 0, and 50 V, respectively. The results in Figure 8c indicate that the memory device using MH-*b*-PStFl₁ as the electret could achieve an $I_{\text{ON}}/I_{\text{OFF}}$ ratio around 10^3 over 180 cycles. On the contrary, the memory device using MH-*b*-PStFl₂ as the electret shows a poor device stability since it loses the switching property after 20 cycles. The poor switching stability of the MH-*b*-PStFl₂-based device is considered to be due to the extremely strong hole-trapping nature of PStFl₂ block. The V_{TH} shifting can be maintained in the negative direction, namely keeping a low drain current at $V_g = 0$ V. Similar behavior has been observed in our previous work.¹⁴ Previously, we also observed that the PStFl₂-only device showed a faster degradation of the ON current compared to the PStFl₁-only devices. It indicated that the polymer with a longer conjugated moiety led to a lower device stability. Therefore, the MH-*b*-PStFl₁-based memory

device is the better candidate for nonvolatile flash-type memory application, rather than the MH-*b*-PStFl₂-based one though it has a stronger hole trapping ability.

CONCLUSIONS

We have successfully prepared the maltoheptaose (MH)-based diblock copolymers MH-*b*-PStFl_{*n*} (*n* = 1 or 2) by the Cu(I)-catalyzed click reaction between ethynyl-terminated maltoheptaose and azido-terminated PStFl_{*n*}. MH-*b*-PStFl_{*n*} in thin films with thickness around 50 nm was found to self-assemble into sub-10 nm spherical microstructures after thermal treatment according to TEM, AFM, SAXS, and GISAXS measurements. These MH-*b*-PStFl_{*n*}-made thin films were directly used as the polymer electret layer and sandwiched between pentacene and SiO₂ layers to fabricate OFET-type memory devices. These fabricated OFET-type memory devices showed an outstanding memory performance with the high $I_{\text{ON}}/I_{\text{OFF}}$ ratios (10^6 – 10^8) and a long-term retention time greater than 10^4 s. For MH-*b*-PStFl₁-based memory devices, the write–read–erase–read (WRER) cycles could be repeated more than 180 cycles. In addition, this study also demonstrated that the memory characteristics of the above MH-*b*-PStFl_{*n*}-based memory devices could be well tuned by factors in terms of the fabrication process, thin film morphology, and π -conjugation length of the pendent group. As a perspective, the MH-*b*-PStFl_{*n*}-based memory device is a promising candidate for green electronics as nonvolatile flash memory applications.

ASSOCIATED CONTENT

Supporting Information

OFET characteristics of pentacene-based memory devices using the MH-*b*-PStFl_{*n*} electrets; ¹H NMR spectra of ethynyl-MH, PStFl₁-Br, PStFl₁-N₃, and MH-*b*-PStFl₁; FTIR spectra of ethynyl-MH, PStFl₁-Br, PStFl₁-N₃, and MH-*b*-PStFl₁; TGA

and DSC curves of ethynyl-MH, PStFl₁-N₃, and MH-*b*-PStFl₁; GPC profiles of PStFl_n and MH-*b*-PStFl_n; AFM images and GISAXS patterns of as-cast and solvent-annealed MH-*b*-PStFl_n; UV-vis spectra, CV, and energy level diagram of ethynyl-MH, PStFl₁-Br, and PStFl₁-N₃; *I*–*V* curves and memory characteristics of the devices using MH-*b*-PStFl_n thin films. The Supporting Information is available free of charge on the ACS Publications website at DOI: 10.1021/acs.macromol.5b00651.

AUTHOR INFORMATION

Corresponding Author

*Tel +886-2-23628398; e-mail chenwc@ntu.edu.tw (W.-C.C.).

Notes

The authors declare no competing financial interest.

ACKNOWLEDGMENTS

The authors acknowledge the financial support from Ministry of Science and Technology of Taiwan.

REFERENCES

- (1) (a) Karakawa, M.; Chikamatsu, M.; Yoshida, Y.; Azumi, R.; Yase, K.; Nakamoto, C. *Macromol. Rapid Commun.* **2007**, *28* (14), 1479–1484. (b) Nagashima, K.; Koga, H.; Celano, U.; Zhuge, F.; Kanai, M.; Rahong, S.; Meng, G.; He, Y.; De Boeck, J.; Jurczak, M.; Vandervorst, W.; Kitaoka, T.; Nogi, M.; Yanagida, T. *Sci. Rep.* **2014**, *4*, 5532. (c) Valentini, L.; Cardinali, M.; Fortunati, E.; Kenny, J. M. *Appl. Phys. Lett.* **2014**, *105* (15), 153111. (d) Chiu, Y. C.; Otsuka, I.; Halila, S.; Borsali, R.; Chen, W. C. *Adv. Funct. Mater.* **2014**, *24* (27), 4240–4249. (e) Kafy, A.; Sadashivuni, K. K.; Kim, H. C.; Akther, A.; Kim, J. *Phys. Chem. Chem. Phys.* **2015**, *17* (8), 5923–5931.
- (2) (a) Otsuka, I.; Isono, T.; Rochas, C.; Halila, S.; Fort, S.; Satoh, T.; Kakuchi, T.; Borsali, R. *ACS Macro Lett.* **2012**, *1* (12), 1379–1382. (b) Cushen, J. D.; Otsuka, I.; Bates, C. M.; Halila, S.; Fort, S.; Rochas, C.; Easley, J. A.; Rausch, E. L.; Thio, A.; Borsali, R.; Willson, C. G.; Ellison, C. J. *ACS Nano* **2012**, *6* (4), 3424–3433. (c) Isono, T.; Otsuka, I.; Kondo, Y.; Halila, S.; Fort, S.; Rochas, C.; Satoh, T.; Borsali, R.; Kakuchi, T. *Macromolecules* **2013**, *46* (4), 1461–1469. (d) Isono, T.; Otsuka, I.; Suemasa, D.; Rochas, C.; Satoh, T.; Borsali, R.; Kakuchi, T. *Macromolecules* **2013**, *46* (22), 8932–8940.
- (3) (a) Forrest, S. R. *Nature* **2004**, *428* (6986), 911–918. (b) Heremans, P.; Gelinck, G. H.; Muller, R.; Baeg, K. J.; Kim, D. Y.; Noh, Y. Y. *Chem. Mater.* **2011**, *23* (3), 341–358. (c) Han, S. T.; Zhou, Y.; Xu, Z. X.; Roy, V. A. L.; Hung, T. F. *J. Mater. Chem.* **2011**, *21* (38), 14575–14580. (d) Scott, J. C.; Bozano, L. D. *Adv. Mater.* **2007**, *19* (11), 1452–1463. (e) Leong, W. L.; Mathews, N.; Tan, B.; Vaidyanathan, S.; Dotz, F.; Mhaisalkar, S. *J. Mater. Chem.* **2011**, *21* (14), 5203–5214. (f) Ling, Q.-D.; Liaw, D. J.; Zhu, C.; Chan, D. S.-H.; Kang, E. T.; Neoh, K.-G. *Prog. Polym. Sci.* **2008**, *33* (10), 917. (g) Lin, W. P.; Liu, S.-J.; Gong, T.; Zhao, Q.; Huang, W. *Adv. Mater.* **2014**, *26* (4), 570.
- (4) (a) Baeg, K. J.; Noh, Y. Y.; Ghim, J.; Kang, S. J.; Lee, H.; Kim, D. Y. *Adv. Mater.* **2006**, *18* (23), 3179. (b) Baeg, K. J.; Noh, Y. Y.; Ghim, J.; Lim, B.; Kim, D. Y. *Adv. Funct. Mater.* **2008**, *18* (22), 3678–3685. (c) Sekitani, T.; Yokota, T.; Zschieschang, U.; Klauk, H.; Bauer, S.; Takeuchi, K.; Takamiya, M.; Sakurai, T.; Someya, T. *Science* **2009**, *326* (5959), 1516–1519. (d) Zhang, L.; Wu, T.; Guo, Y. L.; Zhao, Y.; Sun, X. N.; Wen, Y. G.; Yu, G.; Liu, Y. Q. *Sci. Rep.* **2013**, *3*, 9. (e) Kim, S. J.; Lee, J. S. *Nano Lett.* **2010**, *10* (8), 2884–2890. (f) Guo, Y. L.; Di, C. A.; Ye, S. H.; Sun, X. N.; Zheng, J.; Wen, Y. G.; Wu, W. P.; Yu, G.; Liu, Y. Q. *Adv. Mater.* **2009**, *21* (19), 1954–1959.
- (5) (a) Kang, S. J.; Bae, I.; Shin, Y. J.; Park, Y. J.; Huh, J.; Park, S. M.; Kim, H. C.; Park, C. *Nano Lett.* **2011**, *11* (1), 138–144. (b) Nabre, R. C. G.; Asadi, K.; Blom, P. W. M.; de Leeuw, D. M.; de Boer, B. *Adv. Mater.* **2010**, *22* (9), 933–945.
- (6) (a) Chen, C. M.; Liu, C. M.; Tsai, M. C.; Chen, H. C.; Wei, K. H. *J. Mater. Chem. C* **2013**, *1* (12), 2328–2337. (b) Chiu, Y. C.; Chen, T. Y.; Chueh, C. C.; Chang, H. Y.; Sugiyama, K.; Sheng, Y. J.; Hirao, A.; Chen, W. C. *J. Mater. Chem. C* **2014**, *2* (8), 1436–1446. (c) Chou, Y. H.; You, N. H.; Kurosowa, T.; Lee, W. Y.; Higashihara, T.; Ueda, M.; Chen, W. C. *Macromolecules* **2012**, *45* (17), 6946–6956. (d) Chou, Y. H.; Takasugi, S.; Goseki, R.; Ishizone, T.; Chen, W. C. *Polym. Chem.* **2014**, *5* (3), 1063–1071. (e) Lin, J. Y.; Li, W.; Yu, Z. Z.; Yi, M. D.; Ling, H. F.; Xie, L. H.; Li, S. B.; Huang, W. *J. Mater. Chem. C* **2014**, *2* (19), 3738–3743. (f) Chiu, Y. C.; Chen, T. Y.; Chen, Y. G.; Satoh, T.; Kakuchi, T.; Chen, W. C. *ACS Appl. Mater. Interfaces* **2014**, *6* (15), 12780–12788.
- (7) (a) Leong, W. L.; Mathews, N.; Mhaisalkar, S.; Lam, Y. M.; Chen, T. P.; Lee, P. S. *J. Mater. Chem.* **2009**, *19* (39), 7354–7361. (b) Lee, J. S. *Electron. Mater. Lett.* **2011**, *7* (3), 175–183. (c) Chen, C. M.; Liu, C. M.; Wei, K. H.; Jeng, U. S.; Su, C. H. *J. Mater. Chem.* **2012**, *22* (2), 454–461. (d) Chang, H. C.; Liu, C. L.; Chen, W. C. *ACS Appl. Mater. Interfaces* **2013**, *5* (24), 13180–13187.
- (8) Baeg, K. J.; Khim, D.; Kim, J.; Yang, B. D.; Kang, M.; Jung, S. W.; You, I. K.; Kim, D. Y.; Noh, Y. Y. *Adv. Funct. Mater.* **2012**, *22* (14), 2915–2926.
- (9) Sugiyama, K.; Hirao, A.; Hsu, J. C.; Tung, Y. C.; Chen, W. C. *Macromolecules* **2009**, *42* (12), 4053–4062.
- (10) Halila, S.; Manguian, M.; Fort, S.; Cottaz, S.; Hamaide, T.; Fleury, E.; Driguez, H. *Macromol. Chem. Phys.* **2008**, *209* (12), 1282–1290.
- (11) Jeng, U. S.; Su, C. H.; Su, C. J.; Liao, K. F.; Chuang, W. T.; Lai, Y. H.; Chang, J. W.; Chen, Y. J.; Huang, Y. S.; Lee, M. T.; Yu, K. L.; Lin, J. M.; Liu, D. G.; Chang, C. F.; Liu, C. Y.; Chang, C. H.; Liang, K. S. *J. Appl. Crystallogr.* **2010**, *43*, 110–121.
- (12) Frisch, M. J.; Trucks, G. W.; Schlegel, H. B.; Scuseria, G. E.; Robb, M. A.; Cheeseman, J. R.; Montgomery, J., J. A.; Vreven, T.; Kudin, K. N.; Burant, J. C.; Millam, J. M.; Iyengar, S. S.; Tomasi, J.; Barone, V.; Mennucci, B.; Cossi, M.; Scalmani, G.; Rega, N.; Petersson, G. A.; Nakatsuji, H.; Hada, M.; Ehara, M.; Toyota, K.; Fukuda, R.; Hasegawa, J.; Ishida, M.; Nakajima, T.; Honda, Y.; Kitao, O.; Nakai, H.; Klene, M.; Li, X.; Knox, J. E.; Hratchian, H. P.; Cross, J. B.; Bakken, V.; Adamo, C.; Jaramillo, J.; Gomperts, R.; Stratmann, R. E.; Yazyev, O.; Austin, A. J.; Cammi, R.; Pomelli, C.; Ochterski, J. W.; Ayala, P. Y.; Morokuma, K.; Voth, G. A.; Salvador, P.; Dannenberg, J. J.; Zakrzewski, V. G.; Dapprich, S.; Daniels, A. D.; Strain, M. C.; Farkas, O.; Malick, D. K.; Rabuck, A. D.; Raghavachari, K.; Foresman, J. B.; Ortiz, J. V.; Cui, Q.; Baboul, A. G.; Clifford, S.; Cioslowski, J.; Stefanov, B. B.; Liu, G.; Liashenko, A.; Piskorz, P.; Komaromi, I.; Martin, R. L.; Fox, D. J.; Keith, T.; Al-Laham, M. A.; Peng, C. Y.; Nanayakkara, A.; Challacombe, M.; Gill, P. M. W.; Johnson, B.; Chen, W.; Wong, M. W.; Gonzalez, C.; Pople, J. A. *Gaussian 03, Revision B.04*; Gaussian, Inc.: Wallingford, CT, 2004.
- (13) (a) Yoon, J.; Jin, S.; Ahn, B.; Rho, Y.; Hirai, T.; Maeda, R.; Hayakawa, T.; Kim, J.; Kim, K. W.; Ree, M. *Macromolecules* **2008**, *41* (22), 8778–8784. (b) Komiya, H.; Sakai, R.; Hadano, S.; Asaoka, S.; Kamata, K.; Iyoda, T.; Komura, M.; Yamada, T.; Yoshida, H. *Macromolecules* **2014**, *47* (5), 1777–1782.
- (14) Hsu, J. C.; Lee, W. Y.; Wu, H. C.; Sugiyama, K.; Hirao, A.; Chen, W. C. *J. Mater. Chem.* **2012**, *22* (12), 5820–5827.
- (15) (a) Kang, M.; Baeg, K. J.; Khim, D.; Noh, Y. Y.; Kim, D. Y. *Adv. Funct. Mater.* **2013**, *23* (28), 3503–3512. (b) Tsai, T. D.; Chang, J. W.; Wen, T. C.; Guo, T. F. *Adv. Funct. Mater.* **2013**, *23* (34), 4206–4214.
- (16) Baeg, K. J.; Noh, Y. Y.; Sirringhaus, H.; Kim, D. Y. *Adv. Funct. Mater.* **2010**, *20* (2), 224–230.